HHS Public Access

Author manuscript

Ultrasound Med Biol. Author manuscript; available in PMC 2017 September 14.

Published in final edited form as:

Ultrasound Med Biol. 2015 March ; 41(3): 814–831. doi:10.1016/j.ultrasmedbio.2014.10.020.

Contrast-Enhanced Ultrasound Imaging and *In Vivo* Circulatory Kinetics with Low Boiling Point Nanoscale Phase-Change Perfluorocarbon Agents

Paul S. Sheeran[1], **Juan D. Rojas**[1], **Connor Puett**[1], **Jordan Hjelmquist**[2], **Christopher B. Arena**[1], and **Paul A. Dayton**[1,*]

[1]Joint Department of Biomedical Engineering, The University of North Carolina and North Carolina State University, Chapel Hill, NC

[2]Department of Biomedical Engineering, North Carolina State University, Raleigh, NC

Abstract

Many studies have explored phase-change contrast agents (PCCAs) that can be vaporized by an ultrasonic pulse to form microbubbles for ultrasound imaging and therapy. However, few investigations have been published demonstrating the utility and characteristics of PCCAs as contrast agents *in vivo*. In this study, we examine the properties of low boiling point nanoscale PCCAs evaluated *in vivo*, and compare data to conventional microbubbles with respect to contrast generation and circulation properties. In order to do this, we develop a custom pulse sequence to vaporize and image PCCAs using the Verasonics research platform and a clinical array transducer. Results show that droplets can produce similar contrast enhancement to microbubbles (7.29 to 18.24 dB over baseline, depending on formulation), and can be designed to circulate for as much as 3.3 times longer than microbubbles. This study also demonstrates for the first time the ability to capture contrast wash-out kinetics of the target organ as a measure of vascular perfusion.

Keywords

acoustic droplet vaporization; perfluoropropane; perfluorobutane; microbubble; ultrasound; contrast agent; phase change

Introduction

Since their early appearance in patent literature, ultrasonically-activated phase-change contrast agents (PCCAs) have been investigated to solve challenges in both diagnostic and therapeutic applications of ultrasound (Apfel, 1998). PCCAs provide a unique solution in that an externally-applied ultrasonic pulse of sufficient energy can be used to trigger a transition from a liquid state to a gas state – causing a significant change in the size, density, and compressibility of the particle located within tissue. Some of the earliest published studies demonstrated ultrasound-induced phase transition of superheated

*Corresponding Author, padayton@email.unc.edu, Address: 304 Taylor Hall, CB 7575, Chapel Hill, NC 27599, Phone: (919) 843-9521, Fax: (919) 843-9520.

dodecafluoropentane microdroplets *in vitro* and termed the phenomenon ‘acoustic droplet vaporization’ (Kripfgans et al., 2000; Miller et al., 2000). Continued studies showed the utility of this new class of agents in applications such as occlusion therapy, aberration correction, and cavitation enhancement (Kripfgans et al., 2002; Miller and Song, 2002; Miller et al., 2000).

Since these early experiments, the number of preclinical investigations using PCCAs has increased dramatically and expanded to applications spanning diagnostic/molecular imaging, drug/gene delivery, and tissue ablation (Lin and Pitt, 2013; Rapoport, 2012; Sheeran and Dayton, 2012; Wilson et al., 2013). These studies have shown that the ability to activate agents selectively *in vivo* can be useful in overcoming some of the limitations of conventional microbubble contrast agents. One of the most sought-after goals in PCCA literature has been to create agents with small initial size (in the liquid state) and longer circulation times compared to microbubbles in order to allow passive accumulation in solid tumors via the enhanced permeability and retention (EPR) effect (Campbell, 2006; Kopechek et al., 2013; Rapoport et al., 2009; Reznik et al., 2011; Sheeran et al., 2011b; Williams et al., 2013). Once vaporized to form microbubbles, the contrast present could be used to gain diagnostic information about the interstitial environment. Other studies have shown that vaporization of larger, microscale PCCAs may be useful for creating bubbles that become lodged in the vascular network and serve as references for phase aberration correction (Haworth et al., 2008). PCCAs may also be useful in ultrasound molecular imaging for eliminating the need to discriminate between circulating and molecularly targeted agents (Sheeran et al., 2013b). Once activated in a volume of interest, targeted agents will appear as stationary bubbles, while untargeted agents will clear from the imaging plane. Because the un-vaporized droplets remaining in circulation provide very low contrast relative to tissue, the level of molecular expression can be measured immediately. Some studies have demonstrated that the contrast from the newly-created bubbles can be used to aid in therapeutic goals (Couture et al., 2012; Zhang et al., 2010), and potentially with more control over spatial confinement of the effect compared to typical ultrasound contrast agents (Chen et al., 2013).

Perfluorocarbons have proven to be ideal compounds for use with phase-change contrast agents, given their low solubility in aqueous media, relatively high molecular weight, boiling points near physiologic temperatures, and an extensive history of use in medical imaging (Mattrey, 1994; Sheeran and Dayton, 2012). Despite a few studies demonstrating the imaging contrast produced by vaporized perfluorocarbon droplets (Kripfgans et al., 2005, 2002, 2000; Williams et al., 2013), PCCAs have primarily been tested as tools to enhance therapeutic ultrasound. This preference most likely reflects the unique therapeutic opportunities provided by the dramatic change in agent properties with vaporization, as well as technological barriers that have, until recently, limited their use as diagnostic agents.

Although the theoretical expansion of perfluorocarbon droplets is 3 to 6 times their initial diameter, experiments have shown a size change on the order of 10 to 12 fold, as a result of the inward diffusion of dissolved gases from surrounding fluid (Kripfgans et al., 2000; Sheeran et al., 2011a, 2011b; Shpak et al., 2013). In order to produce ideal contrast-providing bubbles for diagnostic vascular applications, droplet vaporization should produce

microbubbles on the order of 1 to 5 micrometers in diameter (similar to clinical formulations such as Definity; Lantheus Medical Imaging, Billerica MA, USA) to allow for high backscatter as well as safe passage through the microvasculature. As a result, the droplets must be on the order of 100 to 500 nm in diameter. One of the physical barriers to using PCCAs as contrast agents stems from scaling effects as droplet diameters are reduced to the low 100s of nanometers. For large droplets with boiling points near body temperature (such as dodecafluoropentane, boiling point 29°C), the droplets exist in a superheated state upon injection until they either spontaneously vaporize or are vaporized by ultrasound. However, as droplet size diminishes, the Laplace pressure increase resulting from interfacial surface tension elevates the boiling point (Rapoport et al., 2009; Sheeran et al., 2011b), creating what Lin and Pitt refer to as ‘artificial superheat’ (Lin and Pitt, 2013). At very small droplet sizes (such as 100s of nm in diameter), the boiling point elevation is substantial enough to limit the efficiency of vaporization and increase vaporization thresholds (Sheeran et al., 2011b). This Laplace pressure influence is especially deleterious for diagnostic applications of PCCAs: it not only reduces the number of droplets that will vaporize at a given pressure, but may cause recently-vaporized bubbles to re-condense to the droplet state once the ultrasonic pulse has passed (Reznik et al., 2013) - reducing the number of contrast-providing bubbles.

One solution to reduce the vaporization thresholds may be to alter the characteristics of the vaporization pulse – such as altering pulse length and frequency. Previous studies have shown that under certain circumstances, pulse length appears to reduce the energy required for vaporization (Fabiilli et al., 2009; Lo et al., 2007; Williams et al., 2013). However, long pulse lengths will alter the bubble distribution as a result of rectified gas diffusion, bubble destruction, and fusion (Kang et al., 2014; Sheeran et al., 2013a; Shpak et al., 2013). These secondary effects and changes in bubble size distribution are likely to be unwanted for contrast applications, and may also cause unintended interactions with tissue. Alternatively, some of the earliest studies involving PCCAs demonstrated that increasing the ultrasound frequency reduced the pressure required to get a similar level of droplet vaporization (Kripfgans et al., 2000). This effect was confirmed in a number of separate studies (Fabiilli et al., 2009; Williams et al., 2013), and recently revealed to be the result of superharmonic focusing of nonlinear pulses that increases the negative pressure within the droplet (Shpak et al., 2014). However, for the purposes of contrast generation using sub-micron droplets, the frequency-dependence may not be a significant factor, since the focusing effect requires highly nonlinear pulses (i.e. high pressures) and appears to be relatively negligible for droplets much smaller than 1 micrometer in diameter at typical human diagnostic imaging frequencies.

Recent studies by our group have demonstrated that the increase in droplet vaporization threshold at small sizes can be circumvented by using perfluorocarbon species with lower boiling points, such as decafluorobutane (DFB, boiling point −2°C) and octafluoropropane (OFP, boiling point −37°C) (Sheeran et al., 2012, 2011a, 2011b). Because the critical temperatures of these compounds are much closer to body temperature than higher boiling point PFCs, the vapor bubbles formed from activation are less likely to re-condense due to Laplace pressure or the compressional half-cycles of the ultrasound pulse. Though a tradeoff exists between sensitivity to ultrasound (i.e. vaporization threshold) and general droplet

thermal stability, the droplet emulsions can be ‘tuned’ to provide an ideal balance for each application by mixing perfluorocarbon species (Kawabata et al., 2005; Sheeran et al., 2012). Previous studies have shown that condensation techniques can be used to generate stable sub-micron droplets that vaporize to bubbles of ideal size for contrast imaging and that these droplets can be activated at pressures available on typical diagnostic ultrasound machines (Sheeran et al., 2013a, 2013b, 2011a).

To our knowledge, no studies in the literature have explored the development of real-time diagnostic contrast-enhancement sequences based on PCCAs, although some studies have been published demonstrating both activation and imaging from a single imaging transducer (Couture et al., 2012; Sheeran et al., 2013b). As contrast agents, PCCAs require unique ultrasound pulse sequences to optimize diagnostic information. While other approaches are possible, perhaps the simplest is an image/activate/image sequence where the first imaging state is used to gather a pre-activation measurement and the second used to assess the level of contrast generated from an activation state. In the initial liquid state, pre-activation imaging must occur at pressures low enough to avoid droplet activation. When activation is desired (either at intervals or user-triggered), activation should cover the area of interest (pre-designated or operator-designated) and produce droplet vaporization as quickly as possible in the plane or volume – likely through focused pulses to minimize activation elsewhere. For the final imaging state, the imaging pressures must be low enough to not cause further droplet vaporization, and to not disrupt the bubbles produced (unless this is desirable). This post-activation imaging state must also occur quickly enough after the activation to capture contrast before it leaves the imaging plane, although this timing may be more flexible for droplets that are stationary (such as targeted droplets or those in tissue rather than vasculature). Clinical ultrasound scanners typically do not allow the level of pulse sequence customization required to create ideal PCCA-based contrast imaging without manufacturer research agreements. A new generation of highly-customizable ultrasound research platforms made by companies such as Verasonics (Redmond, WA, USA) and Cephasonics (Santa Clara, CA, USA) have allowed researchers to overcome these technological barriers and explore new imaging and processing techniques.

In this study, we use the Verasonics ultrasound platform to develop a custom PCCA-based diagnostic imaging sequence where both activation and imaging are accomplished using a single diagnostic linear array probe at ultrasound conditions at or near FDA guidelines for diagnostic imaging (Barnett et al., 2000). By controlling pulse timing, focusing, and pressure, we capture the contrast enhancement provided by PCCAs. Using the rodent kidney as a vascular target, we demonstrate the ability to evaluate both circulation and wash-out kinetics as a function of perfluorocarbon boiling point, and illustrate the considerations necessary to develop optimal sequences for PCCA contrast enhancement.

Materials and Methods

Contrast Agent Preparation

Perfluorocarbon microbubbles and phase-change contrast agents were prepared using techniques described in detail previously (Sheeran et al., 2012). The microbubbles and PCCA precursor microbubbles were encapsulated in a phospholipid cocktail consisting of a

9:1 M ratio of 1,2-distearoyl-*sn*-glycero-3-phosphocholine (DSPC) and 1,2-distearoyl-sn-glycero-3-phosphoethanolamine-N-methoxy(polyethylene-glycol)-2000 (DSPE-PEG2000). Lipids were purchased from Avanti Polar Lipids (Alabaster, AL, USA). The excipient solution consisted of a 16:3:1 ratio of phosphate-buffered saline (PBS), propylene glycol, and glycerol, producing a total lipid concentration of 1 mg/mL. Both control microbubble samples and PCCA precursor microbubbles were generated by adding 1.5 mL of the lipid solution to a 3 mL glass vial and gas-exchanging the headspace with either decafluorobutane or octafluoropropane gas (Fluoromed, Round Rock, TX, USA) prior to bubble formation via a standard mechanical agitation technique (Vialmix, Bristol-Myers-Squibb, New York, NY, USA).

To form PCCAs from decafluorobutane and octafluoropropane, a microbubble condensation technique was used to convert precursor bubbles (formed as described above) to the liquid state (Sheeran et al., 2012, 2011a). Briefly, the vials of microbubbles with cores composed of DFB or OFP were submerged in an isopropanol bath maintained at a temperature between −8°C and −10°C and swirled gently for approximately 2 minutes. The vials were then connected to an adjustable air-pressure source and the headspace pressure increased until a change in emulsion consistency indicating condensation was observed. For DFB samples, condensation was generally observed due to temperature alone, while OFP samples required on the order of 40–50 psi (275–350 kPa) to achieve condensation as a result of a much lower boiling point. Samples were stored at 4°C for a maximum of 5 hours prior to use for DFB, and a maximum of 2 hours for OFP to avoid variation as a result of thermal instability.

Microbubble size distributions were obtained by measuring 2 μL of microbubble emulsion with an Accusizer 780A (Particle Sizing Systems, Santa Barbara, CA, USA), and statistics averaged for 3 independent microbubble vials to obtain a representative distribution and concentration. PCCAs formed from condensed microbubbles were sized by using a NanoSight NS500 (Malvern Instruments Inc., Westborough, MA, USA) capable of measuring both size distribution and concentration of sub-micron particles. The NanoSight was used to capture six 30-second recordings at a temperature of 23.3°C for each sample with all other settings at default values. DFB and OFP droplet samples were diluted 1/200 in PBS prior to sampling. Measurements produced from each of the six recordings were averaged to produce a representative size distribution and concentration for each sample, and the process repeated for a total of 3 samples of both DFB and OFP droplets.

Droplet Imaging and Activation Pulse Sequence

All imaging and droplet activation was performed using a fully customizable Verasonics research ultrasound platform (Verasonics, Redmond, WA, USA), equipped with an ATL L12-5 38mm 192-element linear array probe (Phillips, Andover, MA, USA). The transducer was calibrated in the free-field using a needle hydrophone (Onda HNA-0400, Sunnyvale, CA, USA) in degassed water. The center 128 elements of the transducer were used for all imaging and activation. The Verasonics hardware was controlled by MATLAB (The MathWorks, Natick, MA, USA) scripts, which allows for simple customization of acoustic parameters. Three different sequences were developed: One for B-mode (anatomical) images, another for droplet activation, and a pulse inversion approach (Simpson et al., 1999)

for contrast-specific imaging. The output of the transducer in each imaging mode was controlled by adjusting the output voltage of the Verasonics hardware using MATLAB scripts.

B-mode—For B-mode anatomical imaging, a plane-wave coherent angular compounding approach (Montaldo et al., 2009) was implemented by delivering 9 MHz, 1-cycle sinusoidal pulses from the ATL L12-5 transducer. The final B-mode images were formed by compounding the envelope detected and beamformed RF signal from 7 transmit-receive frames in which the transmit beam was electronically steered at even angular intervals between the axial and lateral dimensions of the transducer (from −18° to 18°). The beamforming and compounding were performed by Verasonics reconstruction algorithms.

Pulse-inversion—For contrast-specific imaging, a similar coherent angular compounding approach as above was used in which the acquisition at each angle consisted of the RF addition of echoes received from sequential 4.5 MHz, 1-cycle pulses delivered 180° out of phase. The initial positive pulse was followed by a negative pulse after an interval of 105 μs, and each image was constructed from the compounding of all angles. The acquisition time between angles was 205 μs, and the final images were captured at a rate of 10 Hz. The number of compounding angles was reduced to 3 (−18°, 0°, 18°) in order to speed up the data transfer rate and reduce reconstruction time. The Verasonics was set to receive at 9 MHz nominally, although no secondary filtering was performed to further isolate the 2^{nd} harmonic component.

Activation—Droplet activation was achieved by a series of electronically focused and steered 5 MHz, 2-cycle sinusoidal pulses. The use of focused pulses allowed activation only within the region of the beam where pressures were highest – limiting unwanted activation elsewhere. In these studies, the area of activation was set to a rectangular region of interest (ROI) within the lateral width of the transducer. Focused pulses were delivered uniformly within this region by setting the lateral and axial spacing between each pulse to cover the ROI. The pulses were delivered in a raster-scan style along the rows from left to right, starting with the deepest row in order to prevent shadowing by bubble clouds produced early in the sequence. Inter-pulse delay was set to 50 μs (near the limit of the Verasonics hardware) in order to activate within the ROI as quickly as possible.

Combined Imaging/Activation Sequence—B-mode imaging was first used as an anatomical reference to locate and align the kidney with the activation ROI. Once the kidney was positioned in the desired location, B-mode images of the final kidney placement were captured and stored offline before switching to pulse inversion and droplet activation modes (Figure 1). Kidney motion due to breathing could result in droplet activation in a plane not aligned with the imaging plane, and therefore a two-trigger structure was developed to ensure alignment between activation and imaging planes. Kidney appearance and motion was monitored during the free imaging state, and upon completion of the previous breathing cycle, the operator triggered the pre-activation imaging state. In this state, 10 frames were collected at a frame rate of 10 Hz and then the system returned to a free imaging state to align with breathing motion prior to activation. Once the animal breathing motion ceased, a

second trigger transitioned the machine to the droplet activation sequence. After a 500 μs delay to switch the Verasonics hardware to the activation voltage, focused activation pulses were delivered as described above, completing the entire activation sequence on a short timescale relative to respiratory motion. Upon completion of the last focused pulse, a delay of 1.2 ms allowed the Verasonics hardware time to return to imaging output levels. After this pause, the machine entered a post-activation imaging state and collected 100 images at a rate of 10 Hz for droplet groups and 10 images at a rate of 10 Hz for microbubble groups. Data were transferred to the PC controlling the Verasonics after both the pre-activation and post-activation captures for offline analysis. The final design choices for the imaging and activation states both *in vitro* and *in vivo* are reflected in Table 1.

In Vitro Verification

In vitro verification of the droplet activation sequence was performed in an acrylic-walled water bath that contained 4.7 L of degassed water maintained at 37°C by circulating warm water through submerged copper tubing. The transducer was angled to reduce direct ultrasound reflections during droplet activation studies. DFB droplets were dispersed in the water to a concentration of approximately 10^7 droplets/mL, and the water was stirred between experimental runs to redistribute the agents.

Based on preliminary studies, the Verasonics output voltage was set to 18V for all imaging sequences (Table 1). Hydrophone measurements of the spatial pressure distribution resulting from the focused pulses were gathered to correlate with images of microbubble clouds generated. The hydrophone was stepped through the transducer's lateral-axial plane at 0.1 mm intervals using a three-axis motion stage (Newport XPS-RC, Irvine, CA, USA). The maximum peak negative pressures were recorded, and the pressure distributions (beam profiles) were analyzed in MATLAB and combined to form a composite beam map.

At a nominal output voltage of 18V peak-to-peak, the maximum peak negative pressures were 482 kPa and 649 kPa for B-mode and pulse-inversion imaging, respectively. These pressures occurred at a depth of 1.5 cm for B-mode and 1.15 cm for pulse-inversion. As both imaging states were implemented with plane wave transmits, the pressure field was relatively uniform compared to a focused-wave approach. During focused activation pulses, the peak negative pressure was 3.0 MPa at a focal depth of 0.5 cm. Due to the elevational lens, pressure increased with increasing depth to a maximum peak negative pressure of 4.8 MPa at 1.4 cm.

Pulses were delivered at even spacing (user specified) within a rectangular region of interest extending laterally from −6 mm to 6 mm relative to the center of the transducer face and axially from 5 to mm 14 mm. The multi-angle coherent plane-wave compounding with pulse inversion script described above was used to image the microbubble clouds generated *in vitro* by droplet activation following the application of focused ultrasound (2 cycles at 5 MHz) in the presence of DFB. Results from these tests were used to set the axial and lateral activation pulse spacing for *in vivo* studies based on the assumption that pulse pressures and spacing adequate to activate DFB *in vivo* would produce even greater activation of OFP droplets – ensuring the ability to measure both agents.

Animal Imaging Protocol

Fischer 344 rats (Charles River laboratories, Wilmington, MA, USA) were used in this study and protocols approved by the University of North Carolina School of Medicine's Institutional Animal Care and Use Committee were followed. Three groups were included in the study: DFB droplets (N = 7), OFP droplets (N = 6), and microbubbles (N = 6). Animals in the microbubbles group were administered DFB microbubbles (the same precursors used to form DFB droplets). All rats were selected based on similar size (~150 g) and age to reduce experimental variation. Rats were anesthetized with 2.5% inhaled isoflurane mixed with room air and their body temperature was maintained using a controllable heating pad. A 24-gauge catheter was inserted into the tail vein for the administration of the agents. The abdomen was shaved and further depilated using a chemical hair remover, and the area to be imaged was coupled to the transducer with water-based acoustic gel.

B-mode imaging was used to locate the kidney within the abdomen. The transducer was moved laterally, axially, and elevationally by a motion stage (Model UTS150PP, Newport-Irvine, CA, USA) until the kidney (transverse plane) aligned with the location of the activation ROI, and anatomical images were then captured. Prior to the injection of contrast agents, the Imaging/Activation program was used to capture agent-free baseline images.

Contrast agents were delivered as single 120 μL bolus doses injected manually followed by a flush of sterile saline, similar to a previous study in mice with DFB droplets (Chen et al., 2013). Based on the contrast agent size distribution and concentration measurements (see Results section), each bolus consisted of 60 μL of contrast agents diluted in 60 μL of saline for an approximate initial blood plasma concentration of 3.99×10^{7} #/mL, 8.42×10^{8} #/mL, and 1.86×10^{9} #/mL for control microbubbles, DFB droplets, and OFP droplets, respectively. Next, the pre-activation and post-activation frames were captured using the imaging/activation sequence every 3 minutes for 19 minutes, starting at 1 minute after the injection for the DFB and OFP groups, and every 2 minutes for 15 minutes, starting 1 minute after the injection for the microbubble group. Animal breathing was monitored closely after the injection and for the remainder of the experiment. The dose of isoflurane was adjusted depending on the breathing rate of the animal.

In Vivo Activation Sequence Parameters

Based on the results of the *in vitro* verification experiments, a lateral spacing between pulses of 0.85 mm (50% of the measured lateral FWHM) and axial spacing of 1.5 mm (500% of the approximate axial FWHM). The area of activation was set to a rectangular region spanning 3 mm to 12 mm axially and from −6 mm to 6 mm laterally relative to the center of the transducer. The change in the axial window between *in vitro* and *in vivo* studies was made in order to ensure the region covered the entire kidney region in this imaging orientation. This combination of ROI and pulse spacing resulted in 90 focused pulses spaced evenly across the region delivered at a rate of 20,000 pulses/s. Transducer output voltage was set to 18V for all imaging sequences, but increased to 30V during the activation sequence to counteract the effects of tissue attenuation. This translated to a free-field peak negative pressure (not accounting for tissue attenuation) of 482.3 kPa and 648.8 kPa during B-mode and pulse-

inversion imaging, respectively (Table 1). The increase in activation voltage resulted in a free-field peak negative pressure of 8.3 MPa (at an axial depth of 1.1 cm).

Data Analysis

Custom MATLAB scripts were used to analyze the pulse inversion data captured with the Verasonics. The output image data (envelope-detected and beam formed) was square root-compressed, so the pixel values in all the frames were squared to obtain the linear beam formed voltage data. In order to analyze the contrast properties within the kidney, reference images were normalized and converted to the decibel scale for visualization. Regions-of-interest (ROIs) were placed manually in the reference image and applied to all frames of the underlying (linear) data set. In cases where shadowing in the images was present, ROIs were drawn to avoid inclusion of the affected pixels. The average pixel value and standard deviation inside the ROI were calculated on each frame of the voltage data.

Contrast Enhancement Measurement—The degree of contrast enhancement was measured by comparing the contrast images with the agent-free baseline in the following sequence. An ROI was placed around the region of highest activation within the kidney in the first post-activation frame (or post-injection, in the case of microbubbles). The mean pixel value was computed for each frame of the entire data set (agent-free baseline, pre-activation, post-activation). For groups that were administered microbubbles, the data set consisted of only the agent-free baseline images and the post-injection images. The agent-free baseline value for each animal was calculated by averaging the ROI values from the 10 agent-free baseline images. The mean pixel value of each frame after administration of the contrast agents was normalized to the agent-free baseline value and converted to decibel scale to arrive at a dB increase in contrast relative to agent-free baseline.

Percentage Filled Measurement—To measure spatial aspects of contrast enhancement, an ROI was drawn around the entire border of the kidney and the mean and standard deviation of the pixel values within the ROI calculated. At each of the contrast measurement time points, the percentage of pixels that exceeded the mean value of the agent-free baseline by at least 3 standard deviations was calculated as a measure of the spatial coverage of the newly generated contrast. Because some pixels in the agent-free case exceed this threshold (due to nonlinear tissue signal), the ‘percent filled’ value was adjusted by subtracting the percentage obtained in the agent-free case. Due to the fundamental physics of ultrasound speckle, as well as the vascular structure of the kidney, the percent filled value should naturally reach a maximum value less than 100.

Half-Life Measurements—Using the contrast enhancement measurements described above, the decrease in the contrast captured with each sequential data set was analyzed to obtain contrast half-lives and quantitatively compare the longevity of agent circulation. The contrast enhancement values of each data set were normalized to the maximum value obtained at the 1 minute time point, and the normalized data for each animal was fitted with an exponential of the form

$$e^{-\beta_h(t-1)}, \quad \text{(Eq. \#1)}$$

where t is the time in minutes after injection, and β_h is the rate of decay. In this fit, any time points were excluded where the mean contrast enhancement captured by the post-activation imaging was not significantly increased compared to the pre-activation imaging. These were excluded due to the fact that the mean contrast should return to zero for the exponential. The contrast measurements capture the maximum signal due to contrast agent enhancement, but once contrast is no longer being produced, this measure will capture the variation in the noise and produce a non-zero value at late time points.

Wash-out Rate Measurements—To measure the rate of contrast clearance from the imaging plane post-activation, the contrast enhancement measurements were clipped to the maximum value (with breathing noise removed) and fit with an exponential curve of the form

$$\mathrm{dB}_{\max} * e^{-\beta_w(t-t_{\max})}, \quad \text{(Eq. \#2)}$$

where β_w is the wash-out rate, t_{max} is the time at which the maximum contrast occurred, and dB_{max} is the maximum contrast enhancement produced.

Results

Contrast Agent Sizing and Concentration

The averaged distribution of DFB microbubbles, which were used as control agents throughout this study, had a mean diameter and variation of distribution of 1.00 ± 0.89 μm, with a mode size of 0.62 μm, and a total concentration of $6.57\times10^9 \pm 0.84\times10^9$ bubbles/mL (N = 3) (Figure 2a). Reproducibility between samples was high, with the standard deviation in the mean of 0.06 μm, and standard deviation in the mode of 0.01 μm (N = 3). Similarly, the precursor microbubbles used to make OFP particles had a mean diameter and variation of distribution of 1.03 ± 0.66 μm, with a mode size of 0.61 μm. OFP microbubbles had a higher mean concentration of $8.50\times10^9 \pm 1.4\times10^9$ bubbles/mL (N = 3) compared to DFB microbubbles, but not significantly so ($p = 0.16$, Student's two-sided t-test).

The representative distributions obtained by averaging all 3 samples of each type of droplet (Figure 2b) produced a mean diameter and distribution variation of 166 ± 59 nm for DFB, with a mode size of 141 nm, and a total concentration of $13.88\times10^{10} \pm 6.58\times10^{10}$ droplets/mL, while OFP produced a mean diameter and distribution variation of 154 ± 64 nm, with a mode size of 110 nm, and a total concentration of $30.61\times10^{10} \pm 9.65\times10^{10}$ droplets/mL. Reproducibility between samples was high, with the standard deviation in the mean less than 3 nm for both OFP (N = 3) and DFB (N = 3). Similarly, mode size of the 3 samples for each droplet type had standard deviations less than 12 nm. A Kolmogorov-Smirnov test showed that the smaller size distribution of OFP droplets was statistically significant compared to DFB ($p < 0.001$), which agreed with Student's two-tailed t-test

evaluation of the measured mean ($p = 0.03$) and mode ($p<0.01$) values for the two droplet types. OFP droplets had a nearly significant increase in concentration compared to DFB ($p = 0.07$), similar to the microbubble concentration results. The smaller mode and mean diameters of the OFP samples can be expected based on ideal gas laws, which predict a greater size-dependent factor of conversion for OFP than DFB (Evans et al., 2006; Sheeran et al., 2014, 2011b). Given that the peak in the DFB microbubble distribution occurred at 0.62 μm and at 0.61 μm for OFP, an assumption of ideal conversion between the gas and liquid states suggests a conversion factor of 5.57 ± 0.33 for OFP and 4.41 ± 0.37 for DFB.

Droplet measurements produced higher concentrations than microbubble measurements, which requires further discussion. A small increase in concentration is expected as a result of the reduction in volume of each PFC agent converting to the liquid state, although in theory this should only result in a decrease in total emulsion volume on the order of 5–10 μL – not explaining the order-of-magnitude difference between droplets and bubble measurements. We hypothesize that the discrepancy is due to the differences in the equipment used to measure the agents. Specifically, the Accusizer is not sensitive to objects smaller than 500 nm in diameter – although the lower limit of the microbubble distribution (Figure 2a) clearly indicates that there must be agents present in this range. This unmeasured content suggests the actual concentration in the microbubble samples is likely higher than the measurements provide. Additionally, empty vesicles present in the solution as a result of the phospholipid preparation may increase the measured concentration to some degree. In previous studies, measurements of the pure phospholipid solution showed a small number of particles were present on the order of 100 nm (Sheeran et al., 2011a). Future studies are needed to determine the degree to which sub-micron concentration measurements are skewed by these vesicles. Regardless, these discrepancies highlight inherent challenges in measuring nanoscale and microscale distributions in order to compare performance.

In Vitro Verification

Testing within an imaging field measuring 1 cm^2 at a depth of 1 cm in a water bath maintained at 37°C and containing a concentration of approximately 10^7 DFB droplets/mL demonstrated a correlation between the focal pressures and the sizes of individual microbubble clouds generated by droplet activation (Figure 3). At the *in vitro* imaging and activation output settings (see Methods section), vaporization of DFB droplets was not observed prior to triggering the focused activation pulses, indicating pressures were low enough to eliminate unintended vaporization. This matches previous *in vitro* measurements showing that efficient DFB activation at frequencies near 5 MHz requires pressures on the order of 2 MPa or greater (Sheeran et al., 2013a).

During focused activation pulses, the focal zones as well as the maximum peak negative pressures achieved within these zones differed depending on the focal depth (Figure 3a) as a result of the elevational lens. Accordingly, the sizes of the microbubble clouds differed as a function of the focal depth (Figure 3b). Converting the output peak negative pressures to Mechanical Index (defined as the PNP in MPa divided by the square root of the center frequency in MHz (Apfel and Holland, 2014)), the maximum MI in the imaging state was 0.3, and the maximum MI in the activation state was 2.1. It is important to note that a

mechanical index of 2.1 is higher than the current regulatory limits of diagnostic ultrasound output (MI = 1.9). In this study, it is evident that DFB droplets can be activated at ultrasound pressures lower than MI = 1.9. For example, in Figure 3b at a focal depth of 0.5 cm, bubble clouds are produced at MI = 1.3, although they are much smaller than those produced using higher pressures.

Even in this relatively small acoustic field, differences in the shapes of the focal zones and associated microbubble clouds can be discerned, demonstrating the consequence of electronically steering the focal beam to reach more lateral targets. As depth increases, the beam angle produces a slightly rotated bubble cloud. Additionally, the elevational lensing results in an increase in the microbubble cloud size with depth. When focused pulses are placed sparsely, such as a lateral separation of 6 mm and axial separation of 4.5 mm, contrast can be generated in isolated regions with no overlap (Figures 3a and 3b). The accumulation of many individual microbubble clouds can fill a region of interest with bubbles (Figures 3c and 3d). Differences in the individual microbubble cloud shapes and sizes as a function of their location in the acoustic field can be appreciated if the activating foci are spaced at 1.2 mm laterally (70% of the measured lateral full-width-half-max) and 2.1 mm axially (700% of the approximate axial full-width-half-max) (Figure 3c). However, a more uniform vaporization field of bubbles can be generated if the activating foci are spaced closer at 0.43 mm laterally (25% of the full-width-half-max) and 0.75 mm axially (250% of the approximate axial full-width-half-max) (Figure 3d). Although this results in a visually confluent region of contrast, it also indicates that the vaporization pulses may be interacting with the bubbles produced from previous pulses.

In Vivo Acoustic Parameters

To transition to *in vivo* verification, a lateral spacing between pulses of 0.85 mm (50% of the measured lateral FWHM) and axial spacing of 1.5 mm (500% of the approximate axial FWHM) was chosen within the 1.08 cm^2 activation region (see Methods section) in order to ensure bubble clouds generated from DFB droplets did not overlap significantly and minimizing exposure of existing bubbles to the higher energy activation pulses. These represent distances in between the spacing presented in Figures 3c and 3d. In our setup using a linear array transducer with an elevational lens, the pulse pressures increased with depth up to the elevational focus. However, this will not necessarily be the case *in vivo*, as frequency-dependent attenuation diminishes the pulse pressure as a function of depth and frequency.

Initial *in vivo* investigations at the same pulse parameters used for *in vitro* verification were not capable of producing contrast from DFB droplets, although they proved sufficient to generate contrast from OFP droplets. In order to counteract tissue attenuation and aberration, transducer voltage was increased to 30V for the focused-wave activation state, but the plane-wave imaging states remained at 18V. In order to estimate the actual *in vivo* pressures at this output voltage, the free-field pressures (see Methods section) were derated by a model assuming 3 mm of superficial soft tissue (attenuation coefficient of 0.6 dB/cm at 1 MHz) followed by kidney tissue (attenuation coefficient of 1.0 dB/cm at 1 MHz). The attenuation coefficients were scaled assuming a frequency dependence of 1.1 ($\alpha=\alpha_0 f^{1.1}$) (Bamber, 2005, 2002; Mast, 2000). With this model, the highest *in vivo* PNPs during the B-mode and pulse-

inversion imaging states were 273.7 kPa (MI = 0.09) and 433.1 kPa (MI = 0.14), respectively (Table 2). During the focused-wave activation state the PNP was 3.7 MPa (MI = 1.65) at a depth of 3 mm (the shallowest pulses near the start of the kidney region). At 10 mm, where the kidney region of most of the test rodents ended, the PNP was 4.2 MPa (MI = 1.89). The highest PNP was 4.5 MPa (MI = 2.01), occurring at a depth of 8.5 mm. The deepest focused pulses in the activation ROI, occurring at 12 mm, produced a PNP of 3.8 MPa (MI = 1.70). Thus, the majority of the focused pulses occurred at mechanical indices below the regulatory limit of 1.9, although the pulses central to the kidney occurred at output levels slightly above MI = 1.9 as a result of the elevational focusing lens.

Contrast Enhancement Measurements

Given the differences in the size distributions of the three types of agents as well as the reported differences in concentrations, matching doses in a number-matched or volume-matched manner is not straightforward. Matching the total number of agents per dose does not necessarily produce the same number of microbubbles in the imaging region, as droplet vaporization is fundamentally stochastic. Matching the volume that PFC occupies in the dose does not reflect the different state of microbubbles and PCCAs. To proceed with these preliminary *in vivo* demonstrations, we chose to use a constant aliquot volume from each sample, as the differences in concentration between OFP and DFB droplets were not statistically significantly. For microbubbles, this same aliquot was chosen with the assumption that the actual microbubble concentration was higher than reported (due to the differences in particle sizing equipment), and with the assumption that a higher droplet concentration may compensate for droplet-to-bubble conversion rate less than 100%.

With these experimental choices, contrast produced from microbubbles, DFB droplets, and OFP droplets was easily captured. For tests involving bubbles (no activation pulse), very little contrast signal (due to artifact) was present prior to injection (Figure 4). After injection, the relatively high dose of bubbles created a strong contrast signal that diminished at each time point until no contrast enhancement was observed (typically between minutes 11 and 15). Similar to the microbubble tests, very little signal was present within the kidneys prior to PCCA injection (Figure 4). After injection of DFB droplets the kidneys produced similar contrast to the agent-free baseline, indicating agents were still in the liquid state and that few, if any, bubbles were present due to spontaneously vaporized droplets. OFP droplets, however, produced some ‘flashing’ contrast after injection during the pre-activation imaging sequences, indicating either spontaneous vaporization to bubbles while in circulation or activation of OFP droplets by imaging pulse pressures (see further discussion below). After the vaporization sequence was triggered at 1 minute post-injection, a high degree of contrast was present in the kidney for both DFB and OFP (Figure 4). DFB droplets created a distinct spatial pattern due to the spacing between the individual vaporization pulses. Subsequent imaging/activation sequences for DFB every 3 minutes up to the final time point at 19 minutes showed a similar spatial pattern with a gradual decrease in the amount of contrast produced. For tests with OFP droplets, a high degree of uniform contrast was present throughout the kidney after the activation pulse was delivered. No spatial patterning was present, indicating a much higher degree of activation and bubble formation. In fact, at early

time points, the contrast present within the kidney was high enough to cause shadowing deep within the kidney that brightened as contrast washed out of the upper imaging plane.

Measuring contrast produced by the microbubble injections inside the ROI produced a steady level of contrast enhancement in the 1 second captures at each time point. Droplets, on the other hand, produced a distinct wash-out phase as the newly generated contrast diffused out of the imaging plane and into the rest of the kidney and circulatory system over the 10 to 20 seconds following the activation sequence. Characterizing the contrast enhancement relative to the agent-free baseline for all frames of the video capture produced a contrast wash-out curve at each major time point (Figure 5). Repeating this measurement at each major time point allows assessment of the change in the level of activation over time, which is directly related to the decay and clearance of the non-activated agents remaining in circulation. In these contrast wash-out curves, breathing motion manifests as dramatic drops in the measured value, as breathing causes translation into a neighboring imaging plane where fewer bubbles exist. In Figure 5, breathing motion artifacts have been manually removed to increase clarity.

Grouping the contrast enhancement results for each animal by agent type allows for further analysis illustrating the fundamental difference in the behavior of the agents. The maximum contrast present in animals prior to microbubble injection (N = 6) (representing the ‘noisiest’ frame in the agent-free video capture) was 0.19 ± 0.10 dB. After injection, microbubbles produced a high degree of initial contrast, with a mean value of 12.63 ± 3.64 dB at the 1 minute time point (Figure 6a). Over the next 10 minutes, the contrast decayed quickly and returned to baseline levels by the 13 to 15 minute time points.

For the droplet groups, the pre-injection measurements were similar to the microbubble test group, with noise in the measurement on the order of less than 1 dB (Figure 6b). After the activation sequence, animals in the DFB test group (N = 7) produced a mean contrast enhancement at 1 minute post-injection of 7.29 ± 3.65 dB over the agent-free baseline. At each sequential time point, the ‘on-demand’ contrast from the activation sequence gradually decreased in magnitude, producing a mean contrast enhancement of 2.27 ± 0.92 dB at the 19 minute mark that could be easily observed in the video sequence. In comparison to DFB droplets and microbubbles, activated OFP droplets produced a high initial contrast enhancement, with a mean value of 18.24 ± 3.14 dB at 1 minute post-injection. Similar to microbubbles, OFP contrast generated from each activation sequence decayed rapidly over the course of 19 minutes. At the 13 minute post-injection time point, contrast produced by OFP had a lower mean value (2.24 ± 1.19 dB) than DFB (3.49 ± 1.78 dB), suggesting the concentration in the bloodstream diminished much more rapidly than DFB. This matches prior *in vitro* experiments demonstrating relatively poor thermal stability of OFP droplets at 37°C (Sheeran et al., 2012).

In all three agent types, the range of values in each group at early time points was high, likely due to differences in attenuation and aberration from animal to animal. These effects not only limit brightness of the contrast captured, but also diminish the ability to produce droplet vaporization at depth. In several of the DFB test cases, the appearance of the contrast varied spatially throughout the kidney, with high activation in the axial line central to the

transducer and reduced activation in the left and right extremities of the kidney. In most cases, these reduced regions of activation corresponded with visible acoustic shadowing from upper layers – highlighting the importance of coupling the transducer to the skin as well as possible for PCCA contrast studies.

To arrive at the contrast enhancement values in Figure 6, measurements were normalized to the mean value of the agent-free baseline images rather than the pre-activation images collected just before application of the vaporization sequence. This choice was based on preliminary studies showing that the pre-activation measurement of OFP agents was influenced by droplet vaporization (Figure 4 and 5b). Thus, normalizing to the pre-activation mean value would have the effect of under-reporting the actual contrast generated by OFP particles at early time points. As a result of this choice, it is possible for a systematic shift in the measurements to occur. It was noticed during testing that the mean value of the pre-activation images at later time points post-injection did not always match the agent-free baseline. For example, while the agent-free baseline had a zero-mean value, at the 19 minute mark the pre-activation images of both DFB and OFP had a mean value on the order of 0.5 dB (Figure 7a). In the agent-free baseline, the maximum ‘noise’ in the contrast measurement (the maximum value of the tissue signal in any frame compared to the mean of all frames) was 0.22 ± 0.08 dB for DFB and 0.22 ± 0.13 dB for OFP. At the 19 minute mark, this increased to a value of 0.44 ± 0.20 dB for DFB and 0.82 ± 0.33 dB for OFP (Figure 7b). Although this type of systematic shift could result from circulating microbubbles created by previous vaporization pulses, the small fraction of bubbles created by each sequence relative to the total blood volume, along with the short circulation time of the microbubbles suggests this is unlikely. Visually, the pre-activation captures at these later time points have the appearance of being completely free of contrast agents. We therefore hypothesize that this is a result of slight shifts in the imaging plane accumulating due to breathing motion over the test period. At the beginning of tests, the transducer was aligned with the most anechoic plane of the kidney, and so any shifts from this plane would result in a general increase in the mean tissue signal.

This bias in the measurements complicates the assessment of contrast enhancement in that the maximum dB level produced at each time point may not actually indicate an increase in contrast as a result of the vaporization pulses. Comparing the contrast produced in the 10 frames just prior to activation with the 10 frames following activation statistically (student’s two-sided paired t-test) correlates well with visual assessment of whether an increase in contrast was produced by the sequence. For DFB, all 7 test subjects had a statistically significant increase in contrast at the 19 minute time point, indicating viable droplets were still present in circulation. For OFP, all subjects had a significant increase in contrast at minutes 1 through 10. However, the number of animals with increases in the contrast measurement dropped to only 3 out of 6 by the 16 minute mark, and 2 out of 6 by the 19 minute mark. This highlights the difference in stability between choices of PFC: at the last time point tested, new contrast was being generated in all animals given DFB droplets, while OFP droplets had cleared from circulation in the majority of animals.

Figure 7b also shows important aspects of OFP performance at early time points. Due to the low vaporization thresholds of OFP and relative thermal instability, contrast is produced

even during the pre-activation imaging, manifesting as bright, temporary ‘flashes’ in the videos (Figure 4). This appears as spikes in the pre-activation contrast measurements (Figure 5b). This may be due to a combination of spontaneously vaporized droplets as well as droplet vaporization due to the pressure of the imaging pulses. In previous in vitro studies, the vaporization threshold of microscale OFP droplets exposed to 8 MHz, 2 cycle pulses proved to be at peak negative pressures on the order of 0.5 MPa (Sheeran et al., 2012). Here, the imaging state reached estimated peak negative pressures in the tissue of 424.2 kPa, and so we hypothesize that this effect is primarily due to imaging pulses that exceed the vaporization threshold of large outlier droplets still in circulation at early time points. This is consistent with preliminary studies using lower imaging pressures, where OFP ‘flashing’ was not observed.

Half-life Measurements

By normalizing the contrast enhancement data to the maximum value, the circulation half-life can be calculated with a mono-exponential fit described in Eq. #1 (Figure 8). Using this analysis, microbubbles had a mean decay rate of 0.22 ± 0.02 min^{-1}, producing a mean circulation half-life of 3.26 ± 0.37 min. The minimum and maximum half-lives in the group were 2.77 min and 3.83 min, respectively. OFP droplets produced similar measurements as microbubbles, with a mean decay rate of 0.20 ± 0.06 min^{-1}. The mean half-life of the group was 3.67 ± 0.37 min, with minimum and maximum half-lives in the group of 2.43 min and 5.51 min, respectively. OFP half-lives were not statistically significantly different compared to the half-lives of the microbubble group ($p = 0.4$, student’s two-tailed t-test). DFB droplets, while initially showing lower contrast than the other two types of particles at the 1 minute time point, produced a significantly slower mean decay rate of 0.07 ± 0.01 min^{-1}. The mean half-life of the group was 10.84 ± 1.63 min, with minimum and maximum half-lives in the group of 8.07 min and 13.02 min, respectively. DFB half-lives were statistically significantly different compared to both microbubbles and OFP droplets ($p << 0.01$).

Percentage of Kidney Filled

Up to this point, all analysis has been based on the mean value of an ROI placed in the area of highest contrast within the kidney, but analyzing the contrast production by other approaches further illustrates the differences between agents. One possibility is to calculate the percentage of pixels in the kidney as a whole that have exceeded a threshold defined by the agent-free case. This measurement takes into account spatial coverage of the contrast rather than overall intensity. Analyzing the data by this process with a pixel threshold of 3 standard deviations above the mean of the agent-free baseline further reveals differences in performance between DFB, OFP, and microbubbles (Figure 9). Circulating microbubbles produced a mean of 45.11 ± 7.88 percent filled, while OFP produced a higher mean of 49.62 ± 5.97 percent filled compared to microbubbles ($p = 0.19$). DFB, though affording longer circulation time, produces a significantly lower mean of 15.69 ± 8.4 percent filled compared to both microbubbles and OFP droplets ($p << 0.01$). These data demonstrate that the contrast produced from phase-change agents can create more complete coverage of the target organ (OFP) or less (DFB) compared to microbubbles, depending on PCCA formulation, concentration, and activation pulse settings. Although not explored in depth here, this

method also allows characterizing microbubble wash-out curves and droplet half-life clearance.

Discussion

Wash-out Measurements

One unexpected aspect of the wash-out curves captured in this study (Figure 5) is the appearance of two distinct phases. In the first phase, typically occurring in the first second following the vaporization sequence, the contrast within the ROI increases until it reaches a maximal value within 1 to 2 dB of the initial value. This increase may be partly due to contrast spreading from the spatial location of the peak pressures into neighboring regions. It may also be a result of bubble growth shortly after vaporization due to intake of ambient gases dissolved in the bloodstream (Kripfgans et al., 2000; Sheeran et al., 2011a, 2011b; Shpak et al., 2013). In the second phase, the contrast decays exponentially as it washes out of the imaging plane and into the rest of the bloodstream. The mechanisms that create this two-phase behavior require further investigation.

The exponential decay portion of these contrast curves affords a unique possibility to measure a wash-out rate of the vascular network in the imaging plane. Because contrast can be generated ‘on-demand’ with PCCAs and monitored in real-time, the clearance rate can be captured and used as an indication of perfusion. This is similar in concept to the destruction-replenishment curves gathered in microbubble-enhanced ultrasound that have been utilized to measure tissue perfusion (Quaia, 2011; Wei et al., 1998). In destruction-replenishment, pressures near the current upper limit of diagnostic ultrasound are used to destroy the microbubbles in the imaging plane, followed by lower imaging pressures to capture contrast reperfusion. Conversely, with a PCCA sequence high pressures are used to generate contrast in the imaging plane rather than destroy it, and lower pressures used to capture wash-out rather than reperfusion.

As a simple demonstration, the wash-out curves produced 1 minute post-injection for DFB and OFP were fitted with the mono-exponential described in Eq. #2. The DFB group produced a mean wash-out rate of 0.17 ± 0.04 sec^{-1}, while OFP produced a mean rate of 0.13 ± 0.03 sec^{-1}. The clearance rates of the two different agents were nearly statistically significant compared to each other ($p = 0.08$), which may be as a result of the differences in the droplet distributions. As DFB droplets are more thermally stable than OFP, it may be that large outlier droplets are present during activation and take longer to clear compared to OFP. Future studies are needed to compare clearance rate as a function of dose, pulse pressures, droplet size distribution, and droplet boiling point to determine possible sources of these differences. For instance, increased pressures and/or choosing droplets with lower vaporization thresholds increases the extent of vaporization in the elevational dimension as well, which may change the measured wash-out rate.

Although the wash-out characteristics here were captured after a single activation sequence spanning the entire region of interest and with similar droplet size distributions, there are many implementations that could be explored in future studies. Beyond measuring differences in perfusion as a function of droplet size, one could create sparse pockets (i.e.

from single pulses) at desired locations and measure the dissipation as an indication of the underlying vasculature. This differs fundamentally from microbubble destruction-replenishment approaches, where microbubbles in the entire imaging volume are destroyed and the measurement depends on the re-perfusion from all neighboring vascularized tissue. It may be much simpler to apply PCCA wash-out measurements to 3D imaging than destruction-replenishment, since a single bolus could be created in the center of the volume of interest and then be tracked as it dissipates. In larger vessels, PCCAs could be vaporized upstream using electronic steering and the microbubble bolus tracked as it passes a target site - allowing measurement of both flow velocity and flow dynamics. This may be a very desirable approach to theranostic applications, such as targeted clot break-up - where a site is evaluated using PCCA perfusion and then treated.

Finally, it is worth noting that in microbubble destruction-replenishment, pressures necessarily must be high enough to cause bubble collapse and signal extinction. In PCCA wash-out curves, however, high pressures are not necessarily required to generate contrast and monitor the wash-out because it is not a requirement to destroy the contrast agents. The pressure and pulse spacing used here are not optimized for OFP, and it may be possible to accomplish these measurements with significantly less energy delivered into tissue. Furthermore, refinements in droplet properties (size distribution, vaporization thresholds) and dosing may produce a balance that minimizes interaction with vasculature.

Limitations and Future Directions

Adverse Reaction Monitoring—In these studies, no animals displayed visible symptoms of distress or breathing difficulties during the tests or in the post-test monitoring (typically 1 – 2 hours following regaining of consciousness). This suggests the bolus doses were well tolerated, although further dose dependence tests that include cardiac monitoring are needed. As a whole, few dose dependence studies are available for PCCAs – especially at nanoscale sizes. In a study with microscale PFC droplets, Zhang *et al.* observed respiratory distress and blood chemistry changes in a canine model at doses of 2×10^9 droplets/kg, and a dose of 3×10^9 droplets/kg (total PFC dose of 0.2 g/kg) was fatal to the animals (Zhang et al., 2011). Here, much higher doses were administered to the rodents per kg – 5.55×10^{10} droplets/kg for DFB droplets and 1.22×10^{11} droplets/kg for OFP droplets, but the size distributions an order of magnitude smaller in diameter produced a substantially lower total PFC dose of approximately 2.12×10^{-4} g/kg for DFB droplets and 3.75×10^{-4} g/kg for OFP droplets.

One of the most important aspects of PCCA vaporization is the possibility of bioeffects to the surrounding vascular network and tissue (Samuel et al., 2012). This may be desirable in some applications of drug delivery and tissue ablation. However, for the purposes of diagnostic/molecular imaging minimal interaction with tissue is vital. Studies are ongoing to assess damage from vaporization of volatile PCCAs and determine the dependence on droplet formulation, size distribution, and pulse parameters.

Influence of Activation on Half-Life Measurements—One aspect that is not well-understood is to what degree the activation of PCCAs at each time point influences future

measurements. We have assumed in this study that the activation/imaging plane of the kidney represents a small fraction of the overall blood space that PCCAs occupy. However, it is possible that the actual contrast half-lives are higher than measured here due to the fact that each activation sequence removes a fraction of the viable droplets. Regardless, the results demonstrate that PCCAs generally have longer circulation properties than microbubbles. Even the most volatile PCCA explored in literature to date - OFP droplets (PFC boiling point of −36.7°C) - exhibited a virtually identical clearance rate to microbubbles, while DFB droplets had more than three times the measured contrast half-life that microbubbles exhibited. This study also demonstrates that PCCAs at relatively similar doses can produce similar contrast properties as clinical microbubble formulations, which matches previous studies exploring the acoustic properties of bubbles produced from PCCAs (Reznik et al., 2014).

Future Implementation—In this preliminary *in vivo* demonstration of PCCA contrast production, a plane-wave approach to imaging was chosen to facilitate speed in imaging and data transfer. In early studies, plane wave transmits allowed investigation of the period following activation on a short timescale (frame rates near 1 kHz) – but it was found that the wash-out kinetics allowed a much slower frame rate to sufficiently capture contrast wash-out. The final frame rate chosen (10 Hz) leaves much room to improve the imaging quality by developing a focused-wave imaging approach. This may allow better visualization of the unique contrast properties of PCCAs and how they depend on the underlying vascular structure.

It is worth noting that portions of this study (free imaging for alignment and breathing motion monitoring) were captured and displayed in real-time on the Verasonics hardware, but that the actual data captures were not displayed in real-time. This was primarily due to the ultimate intent of offline analysis. However, real-time implementation of the entire sequence could be accomplished easily on the Verasonics with simple changes to the scripts - allowing one to trigger vaporization and visually monitor the contrast enhancement. This is conceptually very similar to microbubble destruction-replenishment sequences (except for the activation sequence design), which are currently implemented on pre-clinical and clinical scanners. The measured clearance in the rodent kidney in this study suggests that imaging rates as low as 10 Hz are sufficient to capture the contrast dynamics of these formulations, which is well within the capabilities of current systems for both plane wave and focused imaging approaches.

The performance of the two different PCCA formulations was compared with set imaging and activation parameters in order to evaluate relative differences when the same acoustic settings are chosen. In reality, the pulse sequence should be designed around formulation and intended use (therapeutic vs. diagnostic) of the PCCA. Some of these considerations are highlighted in a recently published investigation performed in parallel to this one (Puett et al., 2014). Here, the acoustic choices resulted in over-activation and unintended vaporization during imaging for OFP droplets, and under-activation of DFB droplets as a result of the drastic differences in droplet boiling point. For OFP, future sequences will require lower imaging pressures and adjustment of pulse pressure and spacing, whereas for DFB it is likely that higher pressures can be used on imaging and activation (or, alternatively, closer

activation pulse spacing). Because of elevational focusing from the transducer used, the peak negative pressures varied highly with depth. This resulted in activation pulses that were lower than the regulatory limits (MI = 1.9) as well as some that exceeded these limits. It is evident from the images both in vitro (Figure 3) and *in vivo* (Figure 4) that activation of DFB and OFP can be accomplished at PNPs below these limits – as contrast is produced at superficial locations where the measured pressures do not exceed these limits. This is consistent with previous *in vitro* studies showing that DFB droplets can be activated optimally with short pulses that do not exceed MI = 1.9 (Sheeran et al., 2013a). In future studies, implementing the entire pulse sequence within regulatory limits might be accomplished by using 1.5 or 2D arrays, or by simply adjusting the output pressure as a function of axial depth through transmit apodization or output voltage.

Conclusions

In this study, we have demonstrated that custom imaging and activation sequences can be developed to produce and capture contrast from perfluorocarbon phase-change contrast agents *in vivo*. These sequences allow for new perfusion measurements based on microbubble wash-out as well as providing a tool for measuring and optimizing the *in vivo* performance of PCCAs as a function of formulation. PCCA-based contrast-enhanced imaging may open the possibility of new diagnostic and theranostic applications based on PCCA technology.

Acknowledgments

This work was supported in part by pilot funds from the Focused Ultrasound Foundation and the National Science Foundation (DMR#1122483). The authors would like to thank Nazar Filonov and the Nanomedicines Characterization Core Facility at UNC for use of nanoparticle sizing equipment, Gloria Nyankima for assistance with data processing scripts. We appreciate the collaboration of Dr. Terry Matsunaga at the University of Arizona in initial development of the nanoemulsion technology described here. PS would like to acknowledge the generous support of the National Science Foundation as the recipient of a graduate fellowship. CBA was supported by a grant from the National Institute of General Medical Sciences, division of Training, Workforce Development, and Diversity under the Institutional Research and Academic Career Development Award, Grant No. K12-GM000678.

References

Apfel, RE. Activatable infusable dispersions containing drops of a superheated liquid for methods of therapy and diagnosis 1998. US Patent. 5840276.

Apfel RE, Holland CK. Gauging the likelihood of cavitation from short-pulse, low-duty cycle diagnostic ultrasound. Ultrasound Med. Biol. 2014; 17:179–185.

Bamber, JC. Ultrasonic Properties of Tissues. In: Duck, FA.Baker, AC., Starritt, HC., editors. Ultrasound in Medicine. Boca Raton, FL: CRC Press/Taylor and Francis; 2002. p. 500

Bamber, JC. Attenuation and Absorption. In: Hill, CR.Bamber, JC., ter Haar, GR., editors. Physical Principles of Medical Ultrasonics. New York, NY: John Wiley & Sons, Inc; 2005. p. 528

Barnett SB, Haar GR, Ter, Ziskin MC, Rott H-D, Duck FA, Maeda K. International recommendations and guidelines for the safe use of diagnostic ultrasound in medicine. Ultrasound Med. Biol. 2000; 26:355–366. [PubMed: 10773365]

Campbell RB. Tumor physiology and delivery of nanopharmaceuticals. Anticancer Agents Med Chem. 2006; 6:503–512. [PubMed: 17100555]

Chen CC, Sheeran PS, Wu S-Y, Olumolade OO, Dayton PA, Konofagou EE. Targeted drug delivery with focused ultrasound-induced blood-brain barrier opening using acoustically-activated nanodroplets. J. Control. Release. 2013; 172:795–804. [PubMed: 24096019]

Couture O, Urban A, Bretagne A, Martinez L, Tanter M, Tabeling P. In vivo targeted delivery of large payloads with an ultrasound clinical scanner. Med. Phys. 2012:39.

Evans DR, Parsons DF, Craig VS. Physical properties of phase-change emulsions. Langmuir. 2006; 22:9538–9545. [PubMed: 17073477]

Fabiilli ML, Haworth KJ, Fakhri NH, Kripfgans OD, Carson PL, Fowlkes JB. The role of inertial cavitation in acoustic droplet vaporization. Ultrason. Ferroelectr. Freq. Control. IEEE Trans. 2009; 56:1006–1017.

Haworth KJ, Fowlkes JB, Carson PL, Kripfgans OD. Towards Aberration Correction of Transcranial Ultrasound Using Acoustic Droplet Vaporization. Ultrasound Med. Biol. 2008; 34:435–445. [PubMed: 17935872]

Kang S-T, Huang Y-L, Yeh C-K. Characterization of Acoustic Droplet Vaporization for Control of Bubble Generation Under Flow Conditions. Ultrasound Med. Biol. 2014; 40:551–561. [PubMed: 24433748]

Kawabata K, Sugita N, Yoshikawa H, Azuma T, Umemura S. Nanoparticles with Multiple Perfluorocarbons for Controllable Ultrasonically Induced Phase Shifting. Jpn. J. Appl. Phys. 2005; 44:5.

Kopechek JA, Park E, Mei C-S, McDannold NJ, Porter TM. Accumulation of phase-shift nanoemulsions to enhance MR-guided ultrasound-mediated tumor ablation in vivo. J. Healthc. Eng. 2013; 4:109–126. [PubMed: 23502252]

Kripfgans OD, Fowlkes JB, Miller DL, Eldevik OP, Carson PL. Acoustic droplet vaporization for therapeutic and diagnostic applications. Ultrasound Med Biol. 2000; 26:1177–1189. [PubMed: 11053753]

Kripfgans OD, Fowlkes JB, Woydt M, Eldevik OP, Carson PL. In vivo droplet vaporization for occlusion therapy and phase aberration correction. Ieee Trans. Ultrason. Ferroelectr. Freq. Control. 2002; 49:726–738. [PubMed: 12075966]

Kripfgans OD, Orifici CM, Carson PL, Ives KA, Eldevik OP, Fowlkes JB. Acoustic droplet vaporization for temporal and spatial control of tissue occlusion: a kidney study. Ultrason. Ferroelectr. Freq. Control. IEEE Trans. 2005; 52:1101–1110.

Lin C-Y, Pitt WG. Acoustic Droplet Vaporization in Biology and Medicine. Biomed Res. Int. 2013; 2013:1–13.

Lo AH, Kripfgans OD, Carson PL, Rothman ED, Fowlkes JB. Acoustic droplet vaporization threshold: effects of pulse duration and contrast agent. Ferroelectr. Freq. Control. IEEE Trans. 2007; 54:933–946.

Mast TD. Empirical relationships between acoustic parameters in human soft tissues. Acoust. Res. Lett. Online. 2000; 1:37.

Mattrey RF. The Potential Role of Perfluorochemicals (PFCS) in Diagnostic Imaging. Artif. Cells, Blood Substitutes Biotechnol. 1994; 22:295–313.

Miller DL, Kripfgans OD, Fowlkes JB, Carson PL. Cavitation nucleation agents for nonthermal ultrasound therapy. J. Acoust. Soc. Am. 2000; 107:3480–3486. [PubMed: 10875392]

Miller DL, Song J. Lithotripter shock waves with cavitation nucleation agents produce tumor growth reduction and gene transfer in vivo. Ultrasound Med. Biol. 2002; 28:1343–1348. [PubMed: 12467861]

Montaldo G, Tanter M, Bercoff J, Benech N, Fink M. Coherent plane-wave compounding for very high frame rate ultrasonography and transient elastography. IEEE Trans. Ultrason. Ferroelectr. Freq. Control. 2009; 56:489–506. [PubMed: 19411209]

Puett C, Sheeran PS, Rojas JD, Dayton PA. Pulse sequences for uniform perfluorocarbon droplet vaporization and ultrasound imaging. Ultrasonics. 2014 In Press.

Quaia E. Assessment of tissue perfusion by contrast-enhanced ultrasound. Eur. Radiol. 2011; 21:604–615. [PubMed: 20927527]

Rapoport N. Phase-shift, stimuli-responsive perfluorocarbon nanodroplets for drug delivery to cancer. Wiley Interdiscip. Rev. Nanomedicine Nanobiotechnology. 2012; 4:492–510. [PubMed: 22730185]

Rapoport NY, Kennedy AM, Shea JE, Scaife CL, Nam KH. Controlled and targeted tumor chemotherapy by ultrasound-activated nanoemulsions/microbubbles. J. Control. Release. 2009; 138:268–276. [PubMed: 19477208]

Reznik N, Lajoinie G, Shpak O, Gelderblom E, Williams R, de Jong N, Versluis M, Burns PN. On the Acoustic Properties of Vaporized Submicron Perfluorocarbon Droplets. Ultrasound Med. Biol. 2014; 37:1271–1279.

Reznik N, Shpak O, Gelderblom E, Williams R, de Jong N, Versluis M, Burns PN. The efficiency and stability of bubble formation by acoustic vaporization of submicron perfluorocarbon droplets. Ultrasonics. 2013; 53:1368–1376. [PubMed: 23652262]

Reznik N, Williams R, Burns PN. Investigation of Vaporized Submicron Perfluorocarbon Droplets as an Ultrasound Contrast Agent. Ultrasound Med. Biol. 2011; 37:1271–1279. [PubMed: 21723449]

Samuel S, Duprey A, Fabiilli M, Bull JL, Fowlkes JB. In vivo microscopy of targeted vessel occlusion employing acoustic droplet vaporization. Microcirculation. 2012; 19:501–509. [PubMed: 22404846]

Sheeran PS, Dayton PA. Phase-change contrast agents for imaging and therapy. Curr. Pharm. Des. 2012; 18:2152–2165. [PubMed: 22352770]

Sheeran PS, Luois S, Dayton PA, Matsunaga TO. Formulation and Acoustic Studies of a New Phase-Shift Agent for Diagnostic and Therapeutic Ultrasound. Langmuir. 2011a; 27:10412–10420. [PubMed: 21744860]

Sheeran PS, Luois SH, Mullin LB, Matsunaga TO, Dayton PA. Design of ultrasonically-activatable nanoparticles using low boiling point perfluorocarbons. Biomaterials. 2012; 33:3262–3269. [PubMed: 22289265]

Sheeran PS, Matsunaga TO, Dayton PA. Phase-transition thresholds and vaporization phenomena for ultrasound phase-change nanoemulsions assessed via high-speed optical microscopy. Phys. Med. Biol. 2013a; 58:4513. [PubMed: 23760161]

Sheeran PS, Matsunaga TO, Dayton PA. Phase change events of volatile liquid perfluorocarbon contrast agents produce unique acoustic signatures. Phys. Med. Biol. 2014; 59:379. [PubMed: 24351961]

Sheeran PS, Streeter JE, Mullin LB, Matsunaga TO, Dayton Pa. Toward ultrasound molecular imaging with phase-change contrast agents: an in vitro proof of principle. Ultrasound Med. Biol. 2013b; 39:893–902. [PubMed: 23453380]

Sheeran PS, Wong VP, Luois S, McFarland RJ, Ross WD, Feingold S, Matsunaga TO, Dayton PA. Decafluorobutane as a phase-change contrast agent for low-energy extravascular ultrasonic imaging. Ultrasound Med Biol. 2011b; 37:1518–1530. [PubMed: 21775049]

Shpak O, Stricker L, Versluis M, Lohse D. The role of gas in ultrasonically driven vapor bubble growth. Phys. Med. Biol. 2013; 58:2523–35. [PubMed: 23528293]

Shpak O, Verweij M, Vos HJ, de Jong N, Lohse D, Versluis M. Acoustic droplet vaporization is initiated by superharmonic focusing. Proc. Natl. Acad. Sci. 2014; 111:1697–1702. [PubMed: 24449879]

Simpson DH, Chien Ting C, Burns PN. Pulse inversion Doppler: a new method for detecting nonlinear echoes from microbubble contrast agents. Ultrason. Ferroelectr. Freq. Control. IEEE Trans. 1999; 46:372–382.

Wei K, Jayaweera AR, Firoozan S, Linka A, Skyba DM, Kaul S. Quantification of Myocardial Blood Flow With Ultrasound-Induced Destruction of Microbubbles Administered as a Constant Venous Infusion. Circulation. 1998; 97:473–483. [PubMed: 9490243]

Williams R, Wright C, Cherin E, Reznik N, Lee M, Gorelikov I, Foster FS, Matsuura N, Burns PN. Characterization of Submicron Phase-change Perfluorocarbon Droplets for Extravascular Ultrasound Imaging of Cancer. Ultrasound Med. Biol. 2013; 39:475–489. [PubMed: 23312960]

Wilson KE, Wang TY, Willmann JK. Acoustic and Photoacoustic Molecular Imaging of Cancer. J. Nucl. Med. 2013; 54:1851–1854. [PubMed: 24187042]

Zhang M, Fabiilli ML, Haworth KJ, Fowlkes JB, Kripfgans OD, Roberts WW, Ives KA, Carson PL. Initial Investigation of Acoustic Droplet Vaporization for Occlusion in Canine Kidney. Ultrasound Med. Biol. 2010; 36:1691–1703. [PubMed: 20800939]

Zhang M, Fabiilli ML, Haworth KJ, Padilla F, Swanson SD, Kripfgans OD, Carson PL, Fowlkes JB. Acoustic Droplet Vaporization for Enhancement of Thermal Ablation by High Intensity Focused Ultrasound. Acad Radiol. 2011; 18:1123–1132. [PubMed: 21703883]

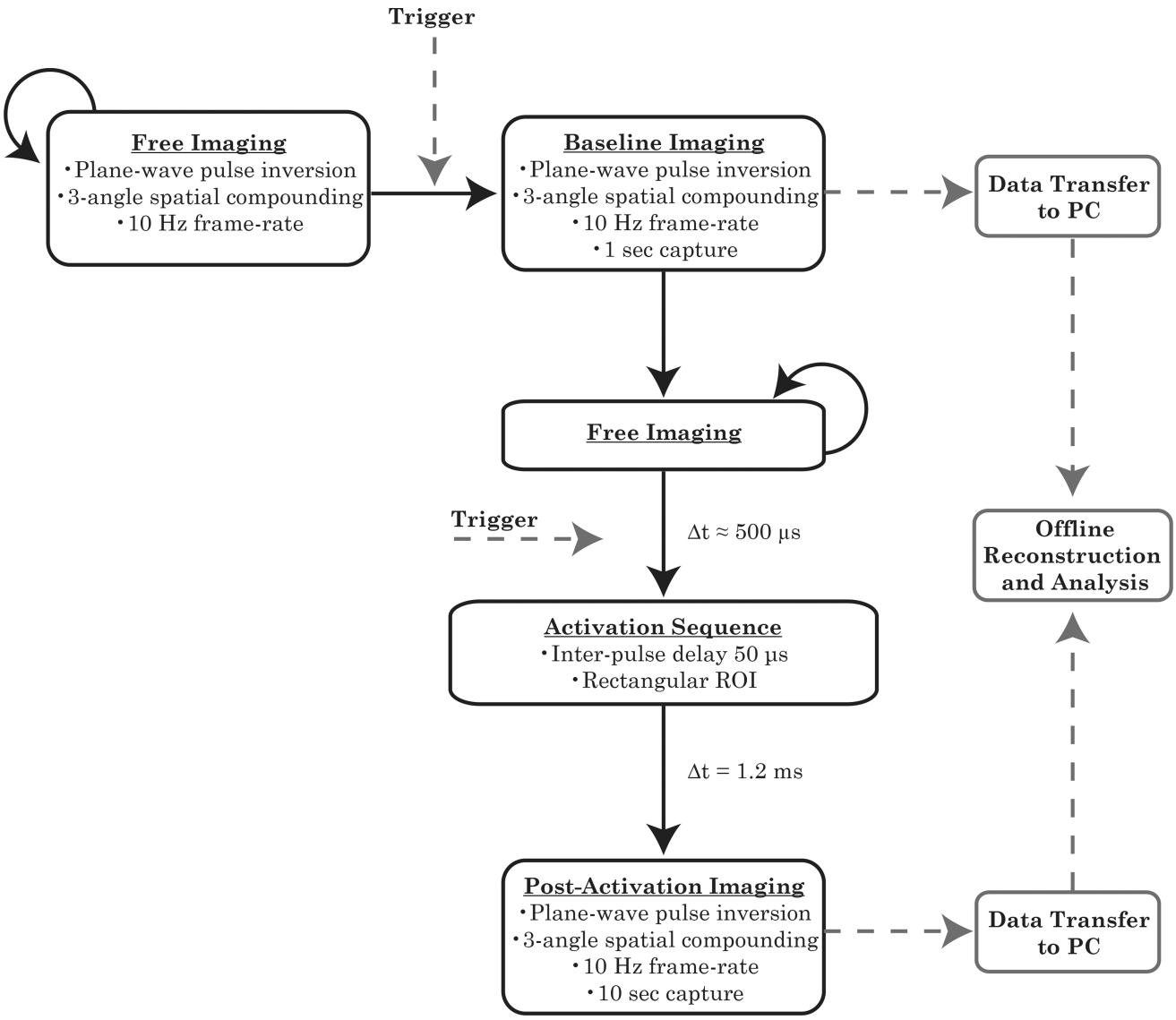

Figure 1.

Imaging and activation sequence. A free imaging state was used to monitor the breathing cycle prior to a manually triggered transition to the pre-activation imaging state. Pre-activation imaging was followed by a return to the free imaging state. After alignment with the breathing cycle, a transition to the activation sequence was manually triggered. A period of post-activation imaging immediately followed the activation sequence. In these studies, images were reconstructed offline after all imaging and data transfer was complete.

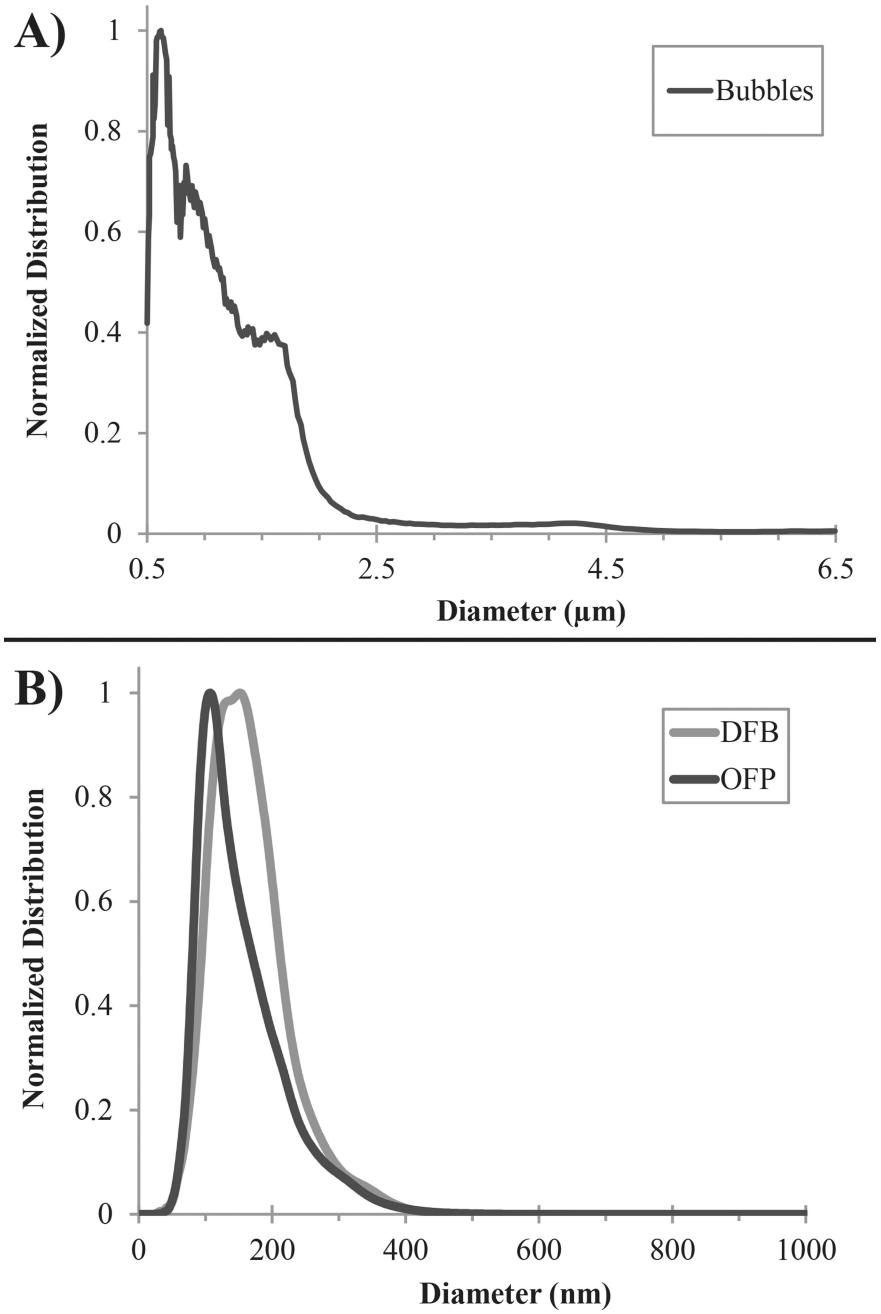

Figure 2.

Representative distributions of contrast agents used in this study. A) DFB microbubbles had a mean diameter of 1.00 ± 0.89 µm and a mode size of 0.62 µm. B) Droplets created by condensing DFB and OFP microbubbles produced sub-micron distributions. DFB droplets had a mean diameter 166 ± 59 nm and a mode of 141 nm, while OFP droplets had a smaller mean diameter of 154 ± 64 nm and a mode of 110 nm.

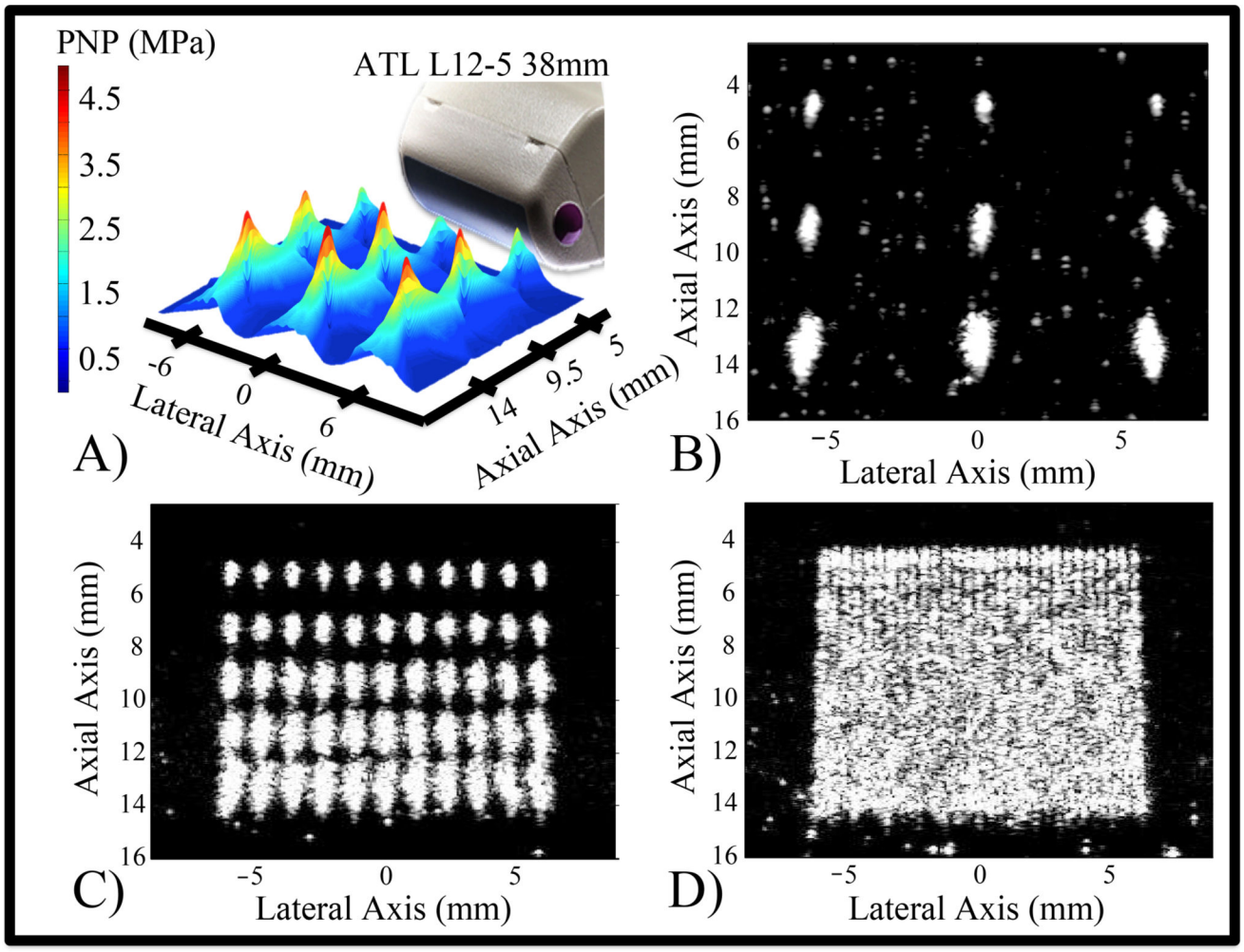

Figure 3.

In Vitro activation of DFB droplets. Changes in the magnitude and geometry of the pressure focal zones (A) and corresponding microbubble clouds (B) at nine focal locations occur as a result of electronically steering the activation pulses. A region of interest can be filled with bubbles by the accumulation of discrete microbubble clouds (C). Spacing the focal locations closer results in a more uniform field of bubbles (D).

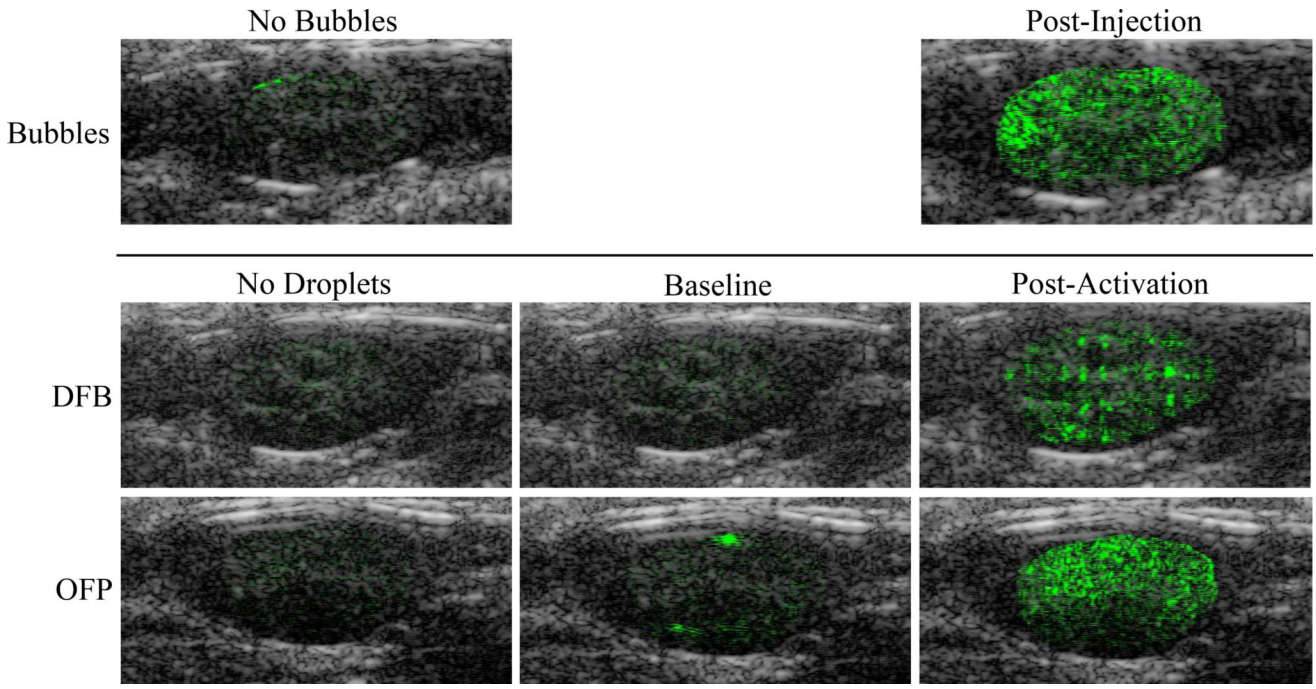

Figure 4.

Example overlays of B-mode (grey scale) ultrasound scans and contrast-specific pulse-inversion scans (green scale) for each contrast agent tested. In all images, the pulse-inversion scans have been manually cropped to the borders of the kidney region to illustrate differences in signal within the kidney. The first column displays the agent-free case (pre-injection), and the second column corresponds to the pre-activation imaging (after injection but before activation). DFB droplets produced no significant increase in contrast after injection, but once activated exhibited a ‘patterned’ contrast appearance with lower mean contrast compared to microbubbles. OFP droplets, in comparison, exhibited some ‘flashing’ in the pre-activation state as a result of unwanted activation, and generated uniform contrast with a higher mean value than microbubbles after the activation sequence. The level of OFP activation was high enough to produce shadowing deep within the kidney at early time points.

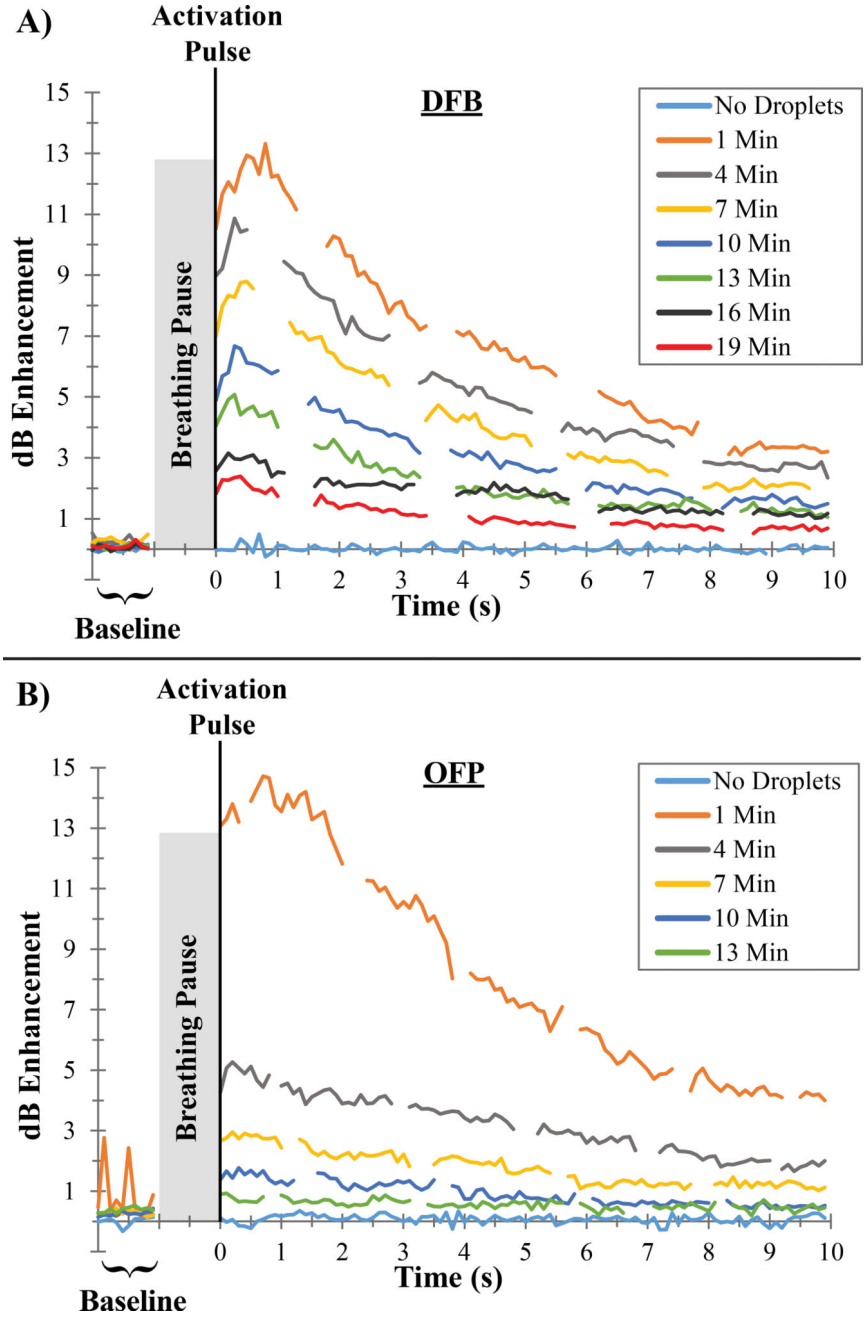

Figure 5.

Examples of contrast measurements taken for individual animals administered A) DFB and B) OFP droplets. The mean value of the contrast enhancement increased over a short period following the vaporization pulse and then decreased as agents washed out of the kidney imaging plane. For OFP droplets, spikes in the 1 minute pre-activation capture are visible caused by unwanted vaporization.

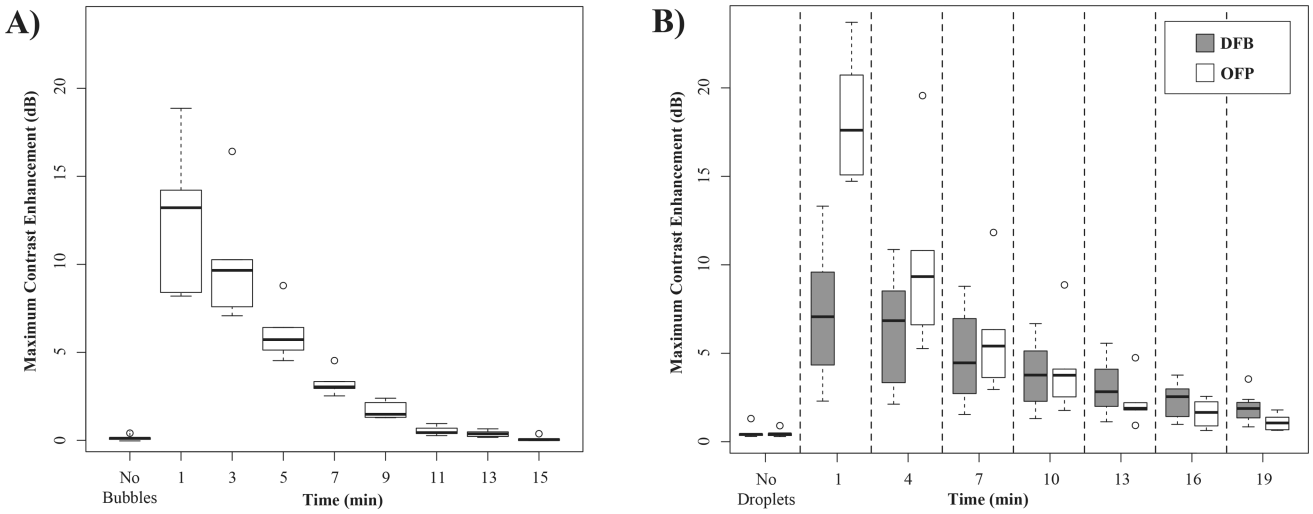

Figure 6.

Maximum dB enhancement relative to the mean of the agent-free baseline for A) microbubbles after injection and B) droplets after application of a vaporization sequence. The mean signal within the manually placed ROI showed that microbubbles produced a high degree of contrast initially that cleared by the 15 minute mark. Contrast generated by activation of OFP was initially greater than DFB and microbubbles, but decayed more rapidly than DFB due to droplet instability. Contrast generation variability in the early time points is largely due to animal-to-animal differences in attenuation and aberration.

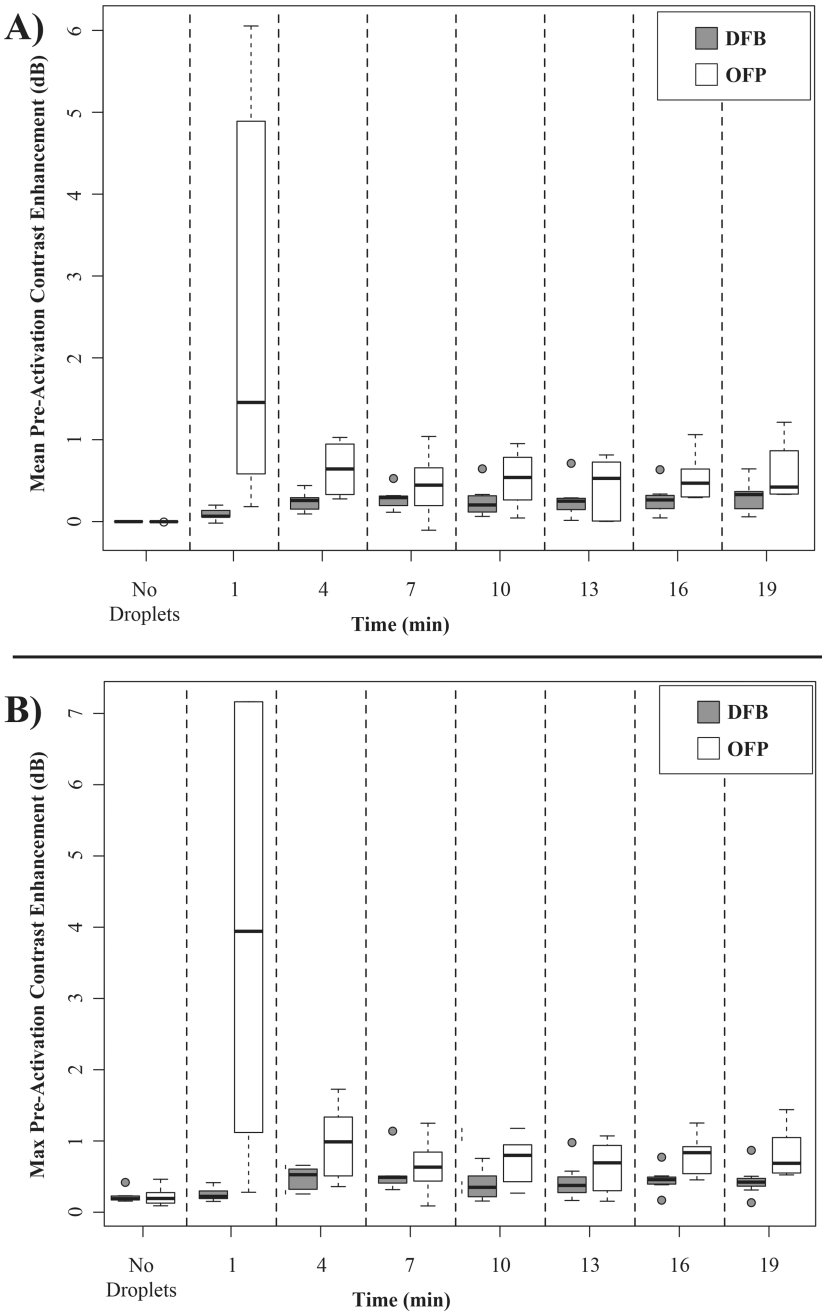

Figure 7.

Change in dB enhancement relative to the mean of the agent-free baseline. A) Initially, the pre-activation signal value is zero-mean, but shifts upward on the order of 0.5 dB over the test period. Similarly, B) the maximum value produced in the video sequence shifts on the order of 0.5 to 1 dB during the test period. It is expected that these changes are due to accumulated shifts in animal positioning over the period. Also visible in A) and B) is the high contrast produced by unwanted activation of OFP droplets at the 1 minute time point.

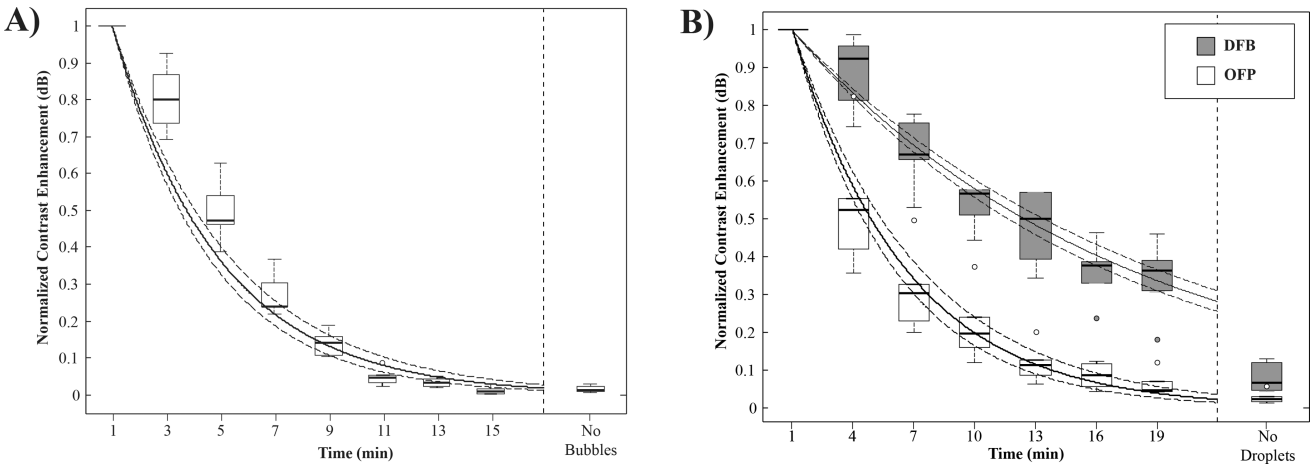

Figure 8.

Maximum contrast enhancement over the mean of the agent-free baseline normalized to the maximum value produced by each animal for A) microbubbles and B) droplets. DFB decayed at a significantly slower rate than OFP and microbubbles, resulting in contrast production half-lives on the order of 3-fold longer than microbubbles and OFP droplets. Shown in solid lines are the exponential curve fits to the grouped data, with 95% confidence intervals in dashed lines.

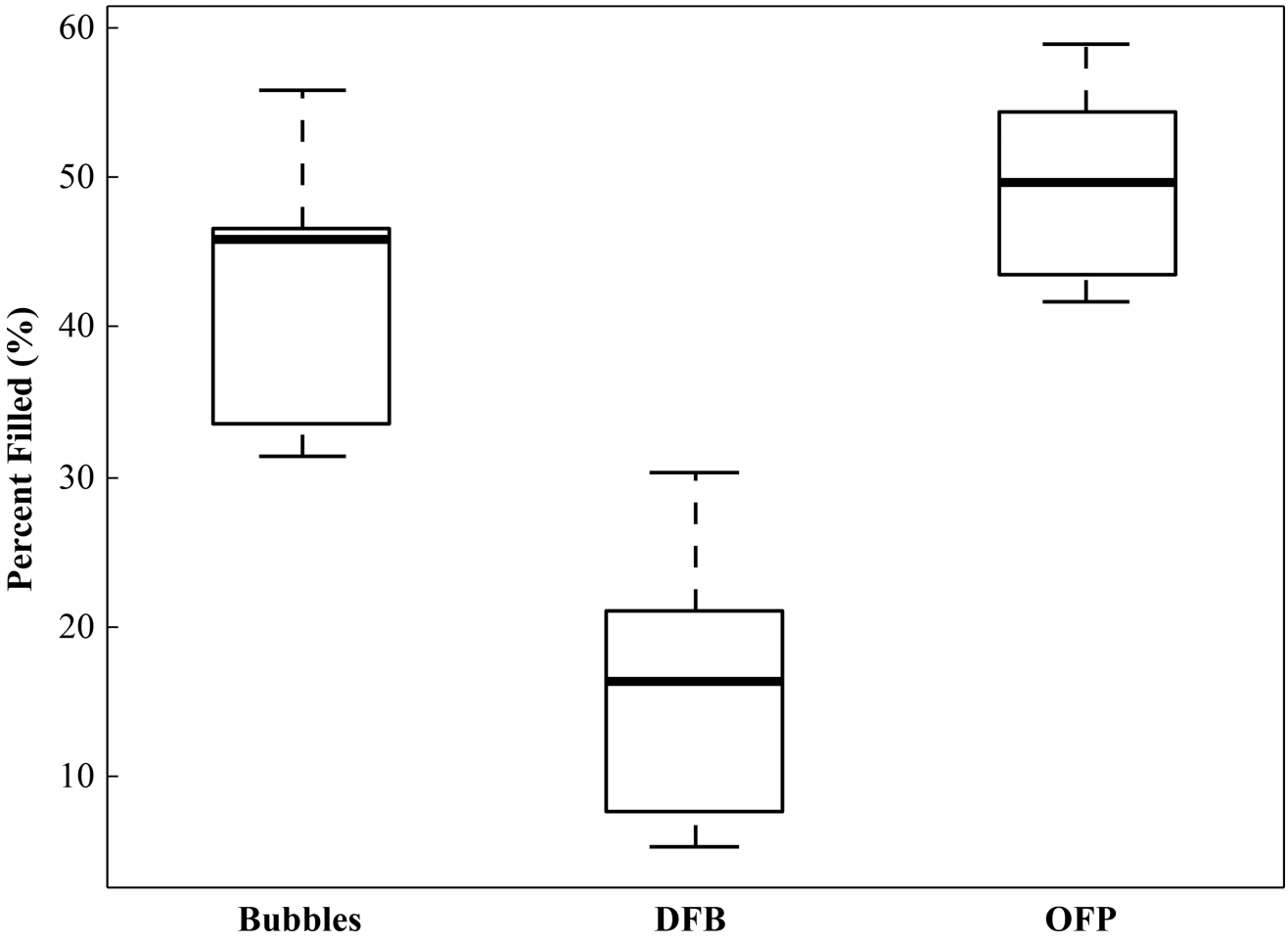

Figure 9.

Calculated percentage of kidney pixels exceeding the agent-free baseline threshold value for the different contrast agents at the 1 minute time point. Contrast generated by the activation of OFP filled a greater percentage of the kidney than a microbubble injection, while activation of DFB droplets produced an irregular contrast generation pattern and filled less of the kidney.

Table 1

Summary of imaging and activation design parameters.

State	Center Freq (MHz)	Pulse Cycles	Compound Angles	Tx volts	Free-field Max PNP Axial Location (cm)	Free-field Max PNP Value (MPa)	Lateral ROI Limits	Axial ROI Limits	Lateral Pulse Separation (mm)	Axial Pulse Separation (mm)
B-mode	9.0	1	7	18	1.50	0.48	-	-	-	-
Pulse Inversion	4.5	1	3	18	1.15	0.65	-	-	-	-
Activation (*in vitro*)	5.0	2	-	18	1.40	4.80	−6mm to 6mm	5mm to 14mm	Various	Various
Activation (*in vivo*)	5.0	2	-	30	1.10	8.30	−6mm to 6mm	3mm to 12mm	0.85	1.50

Ultrasound Med Biol. Author manuscript; available in PMC 2017 September 14.

Table 2

In vivo pressure estimations based on a simple tissue attenuation model.

Estimated *In Vivo* Imaging Pressures			
State	**Max PNP Axial Location (cm)**	**Maximum PNP Value (MPa)**	**Mechanical Index**
B-mode	0.50	0.27	0.09
Pulse Inversion	0.50	0.43	0.14
Estimated *In Vivo* Activation Pressures			
Description	Axial Location (cm)	PNP Value (MPa)	Mechanical Index
Start of Kidney	0.30	3.70	1.65
Maximum PNP	0.85	4.50	2.01
End of Kidney	1.00	4.20	1.89
End of Activation ROI	1.20	3.80	1.70